



31 In order to prevent the spread of COVID-19 pandemic, Chinese government imposed strict  
32 lockdown measures to restraint human activities since 23 January 2020. Primary emissions of air  
33 pollutants experienced dramatic decreases. However, the O<sub>3</sub> concentrations in Tangshan during this  
34 period suffered from substantial increases (143%). On the one hand, the regional transport of  
35 surrounding area promoted local O<sub>3</sub> elevation (30.8 kg/s). On the other hand, the decreases of VOC  
36 concentrations especially alkenes and OVOCs were smaller than NO<sub>x</sub>, and Tangshan was located in  
37 the VOC-limited regime. The overlapping effect led to the dramatic increase of ambient O<sub>3</sub> level in  
38 Tangshan. Therefore, the combined emission reduction of NO<sub>x</sub> and VOCs especially alkenes and  
39 OVOCs is beneficial to mitigate O<sub>3</sub> pollution.

## 40 **1. Introduction**

41 In December 2019, a tragic coronavirus (COVID-19) has spread worldwide causing over 6.33  
42 million deaths as of this writing. In order to combat the further spread of COVID-19, Chinese  
43 government imposed many unconventional and stringent control measures. Nearly all of the  
44 provinces launched full-lockdown responses from 23 January to the early February, 2020.

45 During this period, many strict lockdown measures including the shutdown of industries and  
46 non-essential businesses, curfews, and quarantines necessarily resulted in the reduction of  
47 anthropogenic pollutant emissions. In turn, the dramatic decreases of primary emissions led to  
48 marked changes of air pollutant concentrations. For instance, Zhao et al. (2020) reported that the  
49 concentrations of PM<sub>2.5</sub>, PM<sub>10</sub>, SO<sub>2</sub>, and NO<sub>2</sub> across China decreased by 13.7%, 21.8%, 4.6%, and  
50 46.1%, respectively. Compared with aerosols and gaseous precursors, the concentration decreases  
51 of secondary inorganic ions were not remarkable. Li et al. (2021b) confirmed that the sulfate level  
52 in Tangshan only decreased by 6% after COVID-19 lockdown. Surprisingly, marginal increases in  
53 O<sub>3</sub> were observed in many cities across East China (e.g., Wuhan, Shanghai), which seems to be in  
54 contrast to the changes of most other air pollutants (Saha et al., 2022; Venter et al., 2020). As a  
55 photochemical product, elevated O<sub>3</sub> levels often enhanced the atmospheric oxidation capacity (AOC)  
56 and exerted hazardous impacts on human health and ecosystem (Liu et al., 2022). The exploration  
57 of key driving forces for O<sub>3</sub> pollution has become a hot topic for scientific community. During  
58 COVID-19 period, VOCs and NO<sub>x</sub> levels experienced substantial changes due to strict emission  
59 control measures, and both of these compositions further affected radical chemistry and O<sub>3</sub> change  
60 (Goldberg et al., 2022; Nussbaumer et al., 2022). It provided us an unprecedented opportunity to fill

61 the knowledge gap about the responses of O<sub>3</sub> and radical chemistry to the drastic changes of  
62 precursor emissions, which facilitated the optimization of emission control strategy.

63 It was well known that the O<sub>3</sub> level was often affected by the comprehensive impacts of  
64 meteorological conditions, precursor emissions, and photochemical processes (Li et al., 2022).  
65 Therefore, it is essential to distinguish the contributions of meteorological parameters and emission  
66 change firstly, and then to figure out the O<sub>3</sub> formation mechanisms and sensitivity. Unfavorable  
67 meteorological condition was often considered to be the key factor for the O<sub>3</sub> increase (Yin et al.,  
68 2021; Zhang et al., 2022b). Gong et al. (2018) revealed that daily maximum temperature was major  
69 driving factor responsible for the national O<sub>3</sub> pollution. Besides, RH, WS, and solar radiation also  
70 played significant roles on the O<sub>3</sub> pollution especially in summer and autumn (Chen et al., 2019).  
71 To date, some researchers have employed chemical transport models (CTMs) and statistical models  
72 to distinguish the contributions of meteorological conditions and emission changes to O<sub>3</sub> pollution.  
73 Zhao et al. (2020) utilized Weather Research and Forecasting (WRF) model and the Community  
74 Multiscale Air Quality (CMAQ) model to reveal that the contribution of meteorological factor to O<sub>3</sub>  
75 increase in some megacities (e.g., Beijing, Shanghai, Guangzhou) during COVID-19 period ranged  
76 from 15% to 65%. Later on, Wang et al. (2020b) applied machine-learning models to assess the  
77 contribution of meteorological condition to O<sub>3</sub> pollution in six megacities of China and the result  
78 was in good agreement with study based on CTMs. Unfortunately, these pioneering studies did not  
79 analyze the independent impact of each meteorological parameter on O<sub>3</sub> increase during the  
80 pandemic and the dominant meteorological factor were scarcely revealed. Furthermore, the  
81 contribution of regional transport to O<sub>3</sub> pollution at the fine scale was also less quantified. Compared  
82 with the simple separation of meteorology and emission, the detailed assessment was favorable to  
83 the effective implementation of O<sub>3</sub> pollution prevention policy under the circumstance of different  
84 meteorological conditions.

85 Apart from the impact of meteorological factors, the photochemical processes played important  
86 roles on the ambient O<sub>3</sub>. As a novel technique to analyze the reasons of O<sub>3</sub> pollution, OBMs have  
87 been widely applied to investigate O<sub>3</sub>-VOC-NO<sub>x</sub> relationships and radical chemistry. The method  
88 about O<sub>3</sub> sensitivity to VOCs and NO<sub>x</sub> also have been established to uncover O<sub>3</sub> formation  
89 mechanisms and pollution control strategies. Up to date, many studies have employed this advanced  
90 technique to determine the key formation pathways of ambient O<sub>3</sub>. Liu et al. (2019) analyzed the

91 budget of ambient O<sub>3</sub> in Hong Kong in the autumn of 2007, 2013, and 2016 and found the  
92 contribution of HO<sub>2</sub> + NO only accounted for 56 ± 1 % of the total O<sub>3</sub> production. However, Liu et  
93 al. (2022) estimated that the contribution ratio of HO<sub>2</sub> + NO reached 68 ± 4 % in the autumn of  
94 Xiamen. The O<sub>3</sub> formation pathway varied greatly in different cities and seasons, which might be  
95 strongly dependent on primary emission, the ratio of volatile organic compounds and nitrogen  
96 oxides (VOC/NO<sub>x</sub>), AOC, and radical chemistry. Up to date, most of the current studies focused on  
97 the O<sub>3</sub> formation mechanisms and radical chemistry in summer and autumn, while few studies  
98 clarified the reasons for O<sub>3</sub> pollution events in winter. In fact, winter also suffered from substantial  
99 increase of O<sub>3</sub> concentration such as COVID-19 period. Unfortunately, only Zhang et al. (2022a)  
100 applied this method to determine the source-sink mechanism of atmospheric O<sub>3</sub> during COVID-19  
101 period. Moreover, this study ignored the contributions of alkanes and most alkenes to O<sub>3</sub> pollution.  
102 Although the OFP value of alkanes was generally lower than alkenes and oxygenated volatile  
103 organic compounds (OVOCs), the absolute concentrations of ambient alkanes were often largely  
104 higher than alkenes and OVOCs. Thus, the neglect of alkanes might underestimate the ozone  
105 production and could mislead the diagnosis of ozone sensitivity regimes. In addition, most of the  
106 previous studies focused on O<sub>3</sub> pollution analysis in megacities (e.g., Beijing and Hong Kong) and  
107 coastal cities (e.g., Xiamen), whereas the impact of emission reduction on O<sub>3</sub> pollution and radical  
108 chemistry in a heavy industrial city still remained unknown.

109 As a typical heavy industrial city in NCP, Tangshan possessed many energy-intensive  
110 industries including coal-fired power plants, non-ferrous smelting industries, and cement factories.  
111 According to previous estimates, the anthropogenic VOC emissions in Tangshan reached about 2.35  
112 × 10<sup>5</sup> t yr<sup>-1</sup> (Zhou et al., 2014). Li et al. (2019) further estimated OFP of these released VOCs and  
113 found the total OFP in Tangshan (> 150 Gg-O<sub>3</sub>/grid) in 2017 was significantly higher than those in  
114 most cities over China. Hence, it is highly imperative to clarify local O<sub>3</sub> formation mechanisms and  
115 radical chemistry. Major aims of this study are to clarify (1) the VOCs and O<sub>3</sub> pollution  
116 characteristics after COVID-19 lockdown; (2) the impact of meteorological condition on O<sub>3</sub>  
117 increase in Tangshan; (3) AOC and radical chemistry during pandemic period; and (4) the O<sub>3</sub>  
118 formation mechanisms and sensitivity. The results are expected to offer scientific evidence for  
119 formulating refined ozone management policy.

## 120 **2. Materials and methods**

## 121 2.1 Field measurement

122 The field campaign about the observation of hourly meteorological factors, VOCs, O<sub>3</sub>, and  
123 other gaseous pollutants was performed at a supersite in Tangshan during 1 January-7 February,  
124 2020 (Figure S1). The sampling site was located in the center of urban, Tangshan. It is surrounded  
125 by residential and commercial areas. Some energy-intensive industries were around 50 kilometers  
126 away from this supersite. The meteorological factors including air temperature (T), P, RH, WS, and  
127 wind direction (WD) were measured by a weather station with a sonic anemometer (150WX, Airmar,  
128 USA). O<sub>3</sub>, SO<sub>2</sub>, NO<sub>2</sub>, and CO levels were measured by commercial trace gas analyzer TEI 49i, 43i,  
129 42i, and 48i (Thermo Fisher Scientific, USA), respectively. The HONO concentration was measured  
130 by Monitoring Aerosols and Gases in Ambient Air (MARGA; ADI 2080). A gas chromatography-  
131 mass spectrometer (GC-FID/MS) was applied to monitor at least 50 species of VOC concentrations  
132 with a 1 h time resolution (Table S1). The quality assurance of O<sub>3</sub>, SO<sub>2</sub>, NO<sub>2</sub>, and CO was performed  
133 based on HJ 630-2011 specifications. The limits of detection (LODs), precisions and accuracies of  
134 the VOC analyses were 4-9 ppt, 2%, and 5%, respectively. All of these techniques have been widely  
135 used in previous studies, and some detailed descriptions have been documented in our companion  
136 paper (Li et al., 2021).

## 137 2.2 Deweathered model

138 The ambient O<sub>3</sub> concentration was affected by the comprehensive impacts of meteorological  
139 conditions and emissions. In order to distinguish the separate contributions of emission and  
140 meteorology, a random forest (RF) approach was utilized to serve as the site-specific modeling  
141 platform (Chen et al., 2018). The hourly O<sub>3</sub> level was regarded as the dependent variables, while  
142 the meteorological factors including T, P, RH, WS, and WD, and time predictors (year, day of year  
143 (DOY), day of week (DOW), hour) served as the independent variables. The 10-fold cross-  
144 validation algorithm was applied to examine the performance of this approach. The original dataset  
145 was randomly classified into a training dataset (90% of the original dataset) for developing the RF  
146 model and the remained 10% was regarded as the test dataset. After the establishment of the RF

147 model, the deweathered algorithm was used to estimate the O<sub>3</sub> level at a specific time point (e.g.,  
148 2020/02/05 16:00). The difference of observed O<sub>3</sub> level and deweathered O<sub>3</sub> level was treated as the  
149 concentrations contributed by meteorology. Some typical statistical indexes such as R<sup>2</sup> value, RMSE,  
150 and MAE could be treated as the major criteria to evaluate the modelling performance. In general,  
151 the RF model with the R<sup>2</sup> value higher than 0.50 was considered to be the reliable result. In our  
152 study, some hyperparameters such as the number of trees (ntree), number of samples (nsample) and  
153 the minimal node size in RF model was set as 500, 500, and 5.

### 154 2.3 GAM model

155 The RF model cannot assess the isolated impact of each meteorological parameter on ambient  
156 O<sub>3</sub> concentration. Therefore, the GAM model was further applied to quantify the isolated effect.  
157 The detailed algorithm of the GAM model was as follows:

$$158 \quad g(\mu) = a + \sum f_i(X_i) \quad (1)$$

159 where  $\mu = E(Y|X_1, X_2, \dots, X_m)$ ;  $g(\mu)$  represents the contiguous function;  $f_i$  is the smooth function;  
160  $X_p$  denotes the independent variables.

### 161 2.4 GEOS-Chem model

162 In order to assess the impact of regional transport on O<sub>3</sub> pollution in Tangshan, the GEOS-  
163 Chem model (v12-01) driven by GEOS-FP assimilated meteorological data was employed to  
164 simulate the ambient O<sub>3</sub> level during 1 January-7 February, 2020. The GEOS-Chem model included  
165 detailed ozone-NO<sub>x</sub>-VOC-PM-halogen tropospheric chemistry. The nested grid version of the  
166 model with a horizontal resolution of 0.25° × 0.3125° was used. The anthropogenic emission  
167 inventory in 2019 was collected from Community Emissions Data System (CEDS)(Hoesly et al.,  
168 2018). Then, the emission inventory in 2020 was calculated based on that in 2019 and updated  
169 adjustment factor proposed by (Doumbia et al., 2021). Natural emissions include open biomass  
170 burning, lightning, and soil release. Open fire emissions from GFED4 in 2019 were used for both  
171 of 2019 and 2020 simulations(Van Der Werf et al., 2017). Lightning NO<sub>x</sub> emission was constrained  
172 by the average of LIS/OTD satellite observations from 1995 to 2013(Hudman et al., 2012; Murray  
173 et al., 2012). The contributions of regional transport to ambient O<sub>3</sub> before and after COVID-19

174 lockdown could be quantified based on this model.

## 175 2.5 Observation-based chemical box model

176 In our study, OBM coupled with MCM v3.3.1 was applied to investigate the O<sub>3</sub> formation  
177 mechanisms and the radical chemistry. More than 6700 chemical species and 17,000 reactions were  
178 included in this model. The observation parameters of the gaseous pollutants including O<sub>3</sub>, SO<sub>2</sub>, CO,  
179 HONO, NO, NO<sub>2</sub>, and VOCs, and meteorological parameters including T, RH, and P were utilized  
180 to constrain the model. In addition, the photolysis frequencies (J values) were also incorporated into  
181 the model, which was calculated as a function of solar zenith angle and altitude based on  
182 Tropospheric Ultraviolet and Visible (TUV) model. Before each simulation, the model was run for  
183 5 d as spin-up to ensure the stable state and modelling reliability. AOC was estimated based on the  
184 following equations:

$$185 \quad AOC = \sum_{i=1} k_{Y_i-X} Y_i X \quad (2)$$

186 where Y<sub>i</sub> represents the targeted pollutants (e.g., CH<sub>4</sub>, VOCs, and CO), X represents key oxidants  
187 (OH, NO<sub>3</sub>, and O<sub>3</sub>), and k<sub>Y<sub>i</sub>-X</sub> denotes the rate constants for the reactions of Y<sub>i</sub> and X.

188 The production reaction of O<sub>3</sub> includes RO<sub>2</sub>+NO and HO<sub>2</sub>+NO, while the removal reaction of  
189 O<sub>3</sub> involves O<sub>3</sub> photolysis, O<sub>3</sub>+HO<sub>2</sub>, O<sub>3</sub>+OH, NO<sub>2</sub>+OH, NO<sub>3</sub>+VOCs, and O<sub>3</sub>+VOCs. The net O<sub>3</sub>  
190 production was equaled to the difference of P(O<sub>3</sub>) and L(O<sub>3</sub>). The detailed equations are as follows:

$$191 \quad P(O_3) = k_1[NO][HO_2] + \sum k_{2i}[NO][RO_2] \quad (3)$$

$$192 \quad L(O_3) = k_3[O_1D][H_2O] + k_4[O_3][HO_2] + k_5[O_3][OH] + k_6[NO_2][OH] + \sum k_{7i}[O_3][VOCs] + 2 \sum k_{8i}[NO_3][VOCs] \quad (4)$$

$$193 \quad N(O_3) = P(O_3) - L(O_3) \quad (5)$$

194 where k<sub>i</sub> is the related reaction rate constant. P(O<sub>3</sub>), L(O<sub>3</sub>), and N(O<sub>3</sub>) denote the production, loss,  
195 and net production rate of ambient O<sub>3</sub>.

196 As the quotient of O<sub>3</sub> change ratio and precursor change ratio, RIR is defined to diagnose the  
197 O<sub>3</sub> sensitivity to precursors. The detailed equation is as follows:

$$198 \quad RIR = \frac{\Delta P(O_3) / P(O_3)}{\Delta Y / Y} \quad (6)$$

199 Where RIR reflects the relative incremental reactivity; Δ denotes the increase rate; Y represents  
200 the precursor of O<sub>3</sub> formation.

201 The index of agreement (IOA) was defined as an index to evaluate the modelling performance  
202 of OBM-master chemical mechanism (MCM). In general, the result could be considered to be robust  
203 when the IOA value was higher than 0.70. The IOA in our study reached 0.78. Thus, the performance  
204 of the OBM-MCM was acceptable. The detailed algorithm of IOA was introduced in Liu et al. (2019)  
205 and Liu et al. (2022).

### 206 **3. Results and discussion**

#### 207 3.1 Overview of observations

208 The temporal variations of meteorological parameters are depicted in Figure 1. During the  
209 whole observation period, the prevailing WD was northwesterly. The hourly average T remained  
210 stable characteristic, while RH, P, and WS increased from 58.4%, 1019 hPa, and 0.91 m/s to 60.4%,  
211 1023 hPa, and 1.26 m/s after COVID-19 lockdown, respectively (Table S2). Compared with the pre-  
212 lockdown period, the concentrations of SO<sub>2</sub>, CO, NO, NO<sub>2</sub>, and total VOCs (TVOCs) decreased by  
213 0.92%, 2.49%, 85.2%, 41.2%, and 41.5% during COVID-19 period, respectively. However, the O<sub>3</sub>  
214 concentration increased by 143% after COVID-19 lockdown. Nearly all of the gaseous pollutants  
215 except O<sub>3</sub> displayed decreasing trend after COVID-19 lockdown. It was assumed that many strict  
216 lockdown measures such as partial or complete closure of international borders and nonessential  
217 businesses, and restricted citizen mobility largely reduced the precursor emissions (Goldberg et al.,  
218 2020; Venter et al., 2020). Besides, the increased RH and WS were beneficial to the secondary  
219 transformation from NO<sub>x</sub> to NO<sub>3</sub><sup>-</sup>, and the diffusion and advection of NO<sub>x</sub>, respectively (Huang et  
220 al., 2021; Li et al., 2021b). Both of these meteorological conditions promoted the decrease of  
221 ambient NO<sub>x</sub> concentration. Compared with NO<sub>x</sub> and TVOCs, SO<sub>2</sub> and CO levels suffered from  
222 slight decreases. It was supposed that home order largely increased the residential emission  
223 (Doumbia et al., 2021; Saha et al., 2022; Zheng et al., 2020), which might offset the decreases of  
224 vehicle and industrial emissions. There are many reasons accounting for the substantial increase of  
225 ambient O<sub>3</sub> concentration. Based on the rough analysis, the ratio of VOC/NO<sub>x</sub> during the business-  
226 as-usual period was around 0.74, which could be defined as the VOC-limited region (Li et al.,  
227 2021a). After COVID-19 lockdown period, the decreasing trend of NO<sub>x</sub> (59.1%) was much higher  
228 than that of TVOCs (41.2), which aggravated the rebound of O<sub>3</sub> concentration. In addition, the  
229 increased P might exacerbate O<sub>3</sub> pollution though T remained stable during COVID-19 period (Chen  
230 et al., 2019; Dong et al., 2020; Wang et al., 2022).

231 The analysis of TVOC variation alone cannot reveal the O<sub>3</sub> increase after COVID-19 lockdown,  
232 the detailed variations of VOC species was necessary. During the whole observation period, alkanes  
233 dominated the TVOC concentration with the hourly average concentration of 34.7±10.6 ppbv.  
234 Following alkanes, the alkenes and OVOCs accounted for 20.3% and 13.2% of TVOC  
235 concentrations, respectively (Figure 2 and S2). Compared with the business-as-usual period, the  
236 concentrations of alkanes, alkenes, aromatics, OVOCs, and other VOC species decreased by 44.5%,  
237 28.0%, 50.4%, 40.9%, and 48.3% after COVID-19 lockdown, respectively. The most significant  
238 drop was found in aromatics, which was similar to the result of Changzhou (Jensen et al., 2021). It  
239 might be associated with the drastic decreases in industrial activities and traffic volumes, which  
240 were major sources of ambient aromatics. As the key indicators of vehicular exhaust and industrial  
241 emission (Song et al., 2020; Zhang et al., 2016), the concentrations of toluene and benzene decreased  
242 by 62.8% and 68.6%, respectively. The result also demonstrated that the substantial decreases of  
243 traffic and industrial emissions were responsible for the significant aromatic decreases. However,  
244 the contribution ratios of VOC species suffered from different variation characteristics. The  
245 contribution ratio of alkanes, alkenes, aromatics, OVOCs, and other VOC species accounting for  
246 TVOC concentrations changed from 55.3%, 18.7%, 4.59%, 13.1%, and 8.23% to 52.5%, 23.0%,  
247 3.90%, 13.3%, and 7.27%, respectively. The result of the increase of alkenes ratio and the decrease  
248 of aromatics ratio was in good agreement with that in Nanjing (Wang et al., 2021). The increase of  
249 fraction of alkenes to TVOCs after COVID-19 lockdown might be linked with the emission source.  
250 It was well known that the alkenes might be derived from gasoline evaporation and petrochemical  
251 industries (Wang et al., 2021; Wang et al., 2020a). Some necessary petrochemical industries were  
252 not closed during the pandemic, which caused the slight decreases of alkenes concentrations.

### 253 3.2 The impact of meteorology on ambient O<sub>3</sub>

#### 254 3.2.1 The isolated contribution of meteorology and emission to ambient O<sub>3</sub>

255 Deweathered O<sub>3</sub> concentration was estimated based on RF model after the normalization of  
256 meteorological parameters. The difference of observed O<sub>3</sub> level and normalized O<sub>3</sub> level represented  
257 the O<sub>3</sub> concentration contributed by meteorology. As shown in Figure 3, the observed and  
258 normalized O<sub>3</sub> concentrations increased from 18.7 ± 4.63 and 25.0 ± 5.75 μg/m<sup>3</sup> to 45.6 ± 8.52  
259 μg/m<sup>3</sup> and 44.3 ± 7.93 μg/m<sup>3</sup> after COVID-19 lockdown, respectively. The ambient O<sub>3</sub> level  
260 increased by 143% during COVID-19 period, and the emission reduction and meteorology

261 contributed to 77% and 66% of this increment, respectively. The result suggested that the excessive  
262 NO<sub>x</sub> emission reduction and the increase of VOC/NO<sub>x</sub> ratio in the VOC-limited region might be the  
263 major factors for the substantial increase of ambient O<sub>3</sub> level during the pandemic. In addition, the  
264 unfavorable meteorological conditions especially the increase of P and WS aggravated the O<sub>3</sub>  
265 pollution (Dong et al., 2020; Ning et al., 2020; Shu et al., 2020).

### 266 3.2.2 The effect of each meteorological parameter on O<sub>3</sub> pollution

267 Although the machine-learning model can quantify the overall contribution of meteorological  
268 conditions to O<sub>3</sub> pollution, the impact of each meteorological parameter on ambient O<sub>3</sub> level still  
269 remained unknown. Therefore, the generalized additive model (GAM) was employed to capture the  
270 complex nonlinear relationships between O<sub>3</sub> and its influencing factors. All of these explanatory  
271 variables including T, RH, P, and WS exerted significant nonlinear impacts on O<sub>3</sub> level at the level  
272 of  $p < 0.01$  and degrees of freedom  $> 1$ , indicating that each factor displayed statistical significance.  
273 The F values could reflect the importance of these variables, and these explanatory variables  
274 followed the order of WS (31.6)  $>$  T (24.6)  $>$  RH (16.3)  $>$  P (3.59). As depicted in Figure S3, T and  
275 RH showed positive and negative correlations with O<sub>3</sub> concentrations, respectively. The result was  
276 in good agreement with Liu et al. (2022). Atmospheric O<sub>3</sub> generally showed the higher  
277 concentrations when P was higher than 1025 hPa or lower than 1018 hPa. Among all of these  
278 meteorological parameters, WS showed the highest variable importance, and the higher WS was  
279 favorable for O<sub>3</sub> regional transport. The GEOS-Chem modelling result also suggested that the  
280 average O<sub>3</sub> flux induced by regional transport after COVID-19 lockdown reached 30.8 kg/s, while  
281 the mean O<sub>3</sub> flux before pandemic only reached -5.62 kg/s. The contribution from regional transport  
282 changed from negative effect to positive effect after COVID-19 lockdown, which largely increased  
283 O<sub>3</sub> level during this period. Overall, the combined effects of regional transport and local  
284 photochemical production might be responsible for the O<sub>3</sub> increase.

## 285 3.3 Chemistry perspective

### 286 3.3.1 OFP variations of VOC species after COVID-19 lockdown

287 The VOC species showed distinct reactivities, and thus the OFP value was applied to assess  
288 the contribution of active VOCs to ambient O<sub>3</sub> formation. The OFP value equals to the concentration  
289 of each VOC species multiplying the ozone formation potential coefficient (MIR). It should be noted  
290 that the OFP value did not represent the absolute concentration of ambient O<sub>3</sub>, it only reflected the

291 potential O<sub>3</sub> from the VOC degradation. The temporal variations of VOC species are depicted in  
292 Figure 4. The total OFP value decreased from 77.2±37.6 to 49.5±26.8 ppb after COVID-19  
293 lockdown, indicating marked decreases of VOC reactivities due to drastic lockdown measures.  
294 Among all of VOC species, the OFP of aromatics (62.6%) experienced the most dramatic decrease  
295 owing to the decline of vehicle and industrial emissions (Doumbia et al., 2021). However, the OFP  
296 values of alkenes and OVOCs only suffered from 31.1% and 34.0% decreases during the pandemic,  
297 respectively. Therefore, the contribution ratios of alkenes and OVOCs to total OFP increased from  
298 55.6% and 23.7% during pre-lockdown period to 59.8% and 24.4% after COVID-19 lockdown,  
299 respectively. At first, alkenes and OVOCs were mainly generated from gasoline evaporation and  
300 secondary formation, respectively (Louie et al., 2013; Maji et al., 2020). Both of these VOC species  
301 were not sensitive to lockdown measures compared with alkanes and aromatics, both of which were  
302 mainly sourced from vehicle emission (Harrison et al., 2021; Mozaffar and Zhang, 2020).  
303 Furthermore, the secondary formation could largely compensate for the decrease in primary  
304 emissions of OVOCs (Huang et al., 2019). Moreover, the enhanced regional transport coupled with  
305 increased AOC was also beneficial to the secondary formation of OVOCs (Huang et al., 2020; Wu  
306 et al., 2020).

307 Overall, it should be noted that the VOC/NO<sub>x</sub> ratio increased from 0.69 to 1.07 after COVID-  
308 19 lockdown because the NO<sub>x</sub> emission suffered from more dramatic decrease during the pandemic.  
309 Meanwhile, the ambient O<sub>3</sub> level also exhibited remarkable increase during the same period. The  
310 result suggested that the control of VOCs rather than NO<sub>x</sub> might be more effective in reducing ozone  
311 level in Tangshan. We further analyzed the contributions of various VOC species to O<sub>3</sub> level, and  
312 found the increases in the contributions of alkenes and OVOCs to TVOCs largely elevated ambient  
313 O<sub>3</sub> level. Therefore, the effective control of alkenes and OVOCs emissions facilitated the O<sub>3</sub>  
314 pollution alleviation.

### 315 3.3.2 AOC and radical chemistry after COVID-19 lockdown

316 In order to further explain the reason for O<sub>3</sub> increase, two cases including pre-lockdown and  
317 lockdown periods were selected to analyze the detailed formation/removal mechanisms of O<sub>3</sub> and  
318 radicals. The IOA value of MCM reached 0.81, indicating the modelling performance was reliable  
319 (Chen et al., 2020). The simulated daytime OH concentration displayed a remarkable increase from  
320 0.60±0.41×10<sup>6</sup> to 1.49±0.98×10<sup>6</sup> molecules cm<sup>-3</sup>. It might be associated with the increased regional

321 transport and solar radiation. Moreover, abundant primary pollutants might react with OH during  
322 business-as-usual period, which decreased the OH level. Meanwhile, we also estimated daytime  
323 AOC before and after COVID-19 lockdown. The result suggested that average daytime AOC  
324 increased from  $0.97 \times 10^6$  molecules  $\text{cm}^{-3} \text{s}^{-1}$  to  $1.34 \times 10^7$  molecules  $\text{cm}^{-3} \text{s}^{-1}$ . The daytime AOC in the  
325 winter of Tangshan was significantly lower than that in autumn of Xiamen ( $6.7 \times 10^7$ ) and summer  
326 of Hong Kong ( $6.2 \times 10^7$ ) (Liu et al., 2022; Xue et al., 2016). It was supposed that the solar radiation  
327 in winter was much lower than that in summer and autumn (Jin et al., 2005; Tang et al., 2010).  
328 However, AOC in our study was significantly higher than that during the same period in Changzhou  
329 (Zhang et al., 2022a). As shown in Figure 5, the contribution of OH to AOC reached 85% during  
330 the whole study period, and thus the higher OH concentration in Tangshan was responsible for the  
331 higher AOC compared with Changzhou.

332 Besides, we further analyzed the reason for OH increase after COVID-19 lockdown from the  
333 perspective of budget. OH was mainly generated from the reaction of  $\text{HO}_2 + \text{NO}$ , accounting for  
334  $61 \pm 10\%$  and  $76 \pm 15\%$  of the total production during pre-lockdown and lockdown periods,  
335 respectively (Figure 6). Following the reaction of  $\text{HO}_2 + \text{NO}$ , the processes of HONO photolysis  
336 accounted for  $36 \pm 9\%$  and  $22 \pm 7\%$  of the total OH production during two cases, respectively. Other  
337 pathways including  $\text{O}(1\text{D}) + \text{H}_2\text{O}$ ,  $\text{O}_3 + \text{VOCs}$ , and  $\text{H}_2\text{O}_2$  photolysis only accounted minor  
338 contribution ( $< 5\%$ ) to OH formation. From the perspective of temporal variation, the formation rate  
339 from  $\text{HO}_2 + \text{NO}$  increased from  $0.68 \times 10^7$  during pre-lockdown period to  $1.57 \times 10^7$  molecules  $\text{cm}^{-3}$   
340  $\text{s}^{-1}$  during the pandemic. It might be associated with the excessive reduction of  $\text{PM}_{2.5}$  concentration  
341 because aerosol particles generally scavenged  $\text{HO}_2$  radicals (Shi and Brasseur, 2020). However,  
342 other formation pathways remained relatively stable characteristics after COVID-19 lockdown. The  
343 result indicated that  $\text{HO}_2 + \text{NO}$  was considered to be the major pathway for the significant increase  
344 of OH level during the pandemic.

345 Apart from the analysis of OH formation process, the change of OH loss pathway could also  
346 play an important role on the OH increase. It was well documented that OH was mainly depleted  
347 by four reactions with CO, VOCs, NO, and  $\text{NO}_2$ . All of the loss reactions of OH during pre-  
348 lockdown period were in the order of  $\text{OH} + \text{NO}$  ( $34 \pm 9\%$ )  $>$   $\text{OH} + \text{NO}_2$  ( $23 \pm 7\%$ ) =  $\text{OH} + \text{VOCs}$   
349 ( $23 \pm 6\%$ )  $>$   $\text{OH} + \text{CO}$  ( $20 \pm 5\%$ ), while the loss pathways of OH after COVID-19 lockdown followed  
350 the order of  $\text{OH} + \text{VOCs}$  ( $43 \pm 11\%$ ) =  $\text{OH} + \text{NO}_2$  ( $22 \pm 8\%$ )  $>$   $\text{OH} + \text{CO}$  ( $18 \pm 6\%$ )  $>$   $\text{OH} + \text{NO}$

351 (17±3%). It should be noted that the contribution of NO to OH loss experienced dramatic decrease  
352 after COVID-19 lockdown because the strict lockdown measures largely decreased NO emission,  
353 which could be treated as a nonnegligible reason for the OH increase during the pandemic. Besides,  
354 we also found that the contribution ratio of OH + VOCs showed slight increase because the  
355 decreasing ratios of VOC species were relatively lower than those of NO<sub>x</sub>.

### 356 3.3.3 The chemical mechanisms for O<sub>3</sub> increase after COVID-19 lockdown

357 The formation and loss pathways of O<sub>3</sub> were depicted in Figure 7. The formation of ambient  
358 O<sub>3</sub> was dominated by RO<sub>2</sub> + NO and HO<sub>2</sub> + NO. In our study, the daytime rate of HO<sub>2</sub> + NO during  
359 pre-lockdown period reached  $2.34 \pm 1.08$  ppb h<sup>-1</sup>, accounting for 61% of the total O<sub>3</sub> production.  
360 The result was consistent with many previous studies because OH radical was the initiator of O<sub>3</sub>  
361 photochemical production. Following the pathway of HO<sub>2</sub> + NO, RO<sub>2</sub> + NO ( $1.48 \pm 0.63$  ppb h<sup>-1</sup>)  
362 was also an important pathway for the O<sub>3</sub> formation, accounting for 39% of the total O<sub>3</sub> production.  
363 After COVID-19 lockdown, the daytime rates of HO<sub>2</sub>+NO and RO<sub>2</sub>+NO exhibited significant  
364 increases by 61% and 53%, respectively. The loss rates of ambient O<sub>3</sub> during pre-lockdown and  
365 lockdown periods showed similar characteristics and they followed the order of NO<sub>2</sub> + OH (59%  
366 and 42%) > O<sub>3</sub> photolysis (27% and 33%) > RO<sub>2</sub> + NO<sub>2</sub> (12% and 23%), whereas other pathways  
367 such as O<sub>3</sub> + OH, O<sub>3</sub> + HO<sub>2</sub>, O<sub>3</sub> + VOCs, and NO<sub>3</sub> + VOCs contributed limitedly. Although both of  
368 P(O<sub>3</sub>) and L(O<sub>3</sub>) displayed increases after COVID-19 lockdown, the increase of total O<sub>3</sub> production  
369 was much higher than that of O<sub>3</sub> loss. Thus, the net production rate of O<sub>3</sub> increased from  $2.78 \pm 1.29$   
370 to  $4.58 \pm 1.74$  ppb h<sup>-1</sup> after COVID-19 lockdown, which fully explained the rapid increase of  
371 ambient O<sub>3</sub> level during the pandemic. Compared with the previous studies, the net production rate  
372 of O<sub>3</sub> was much lower than those in summer or autumn of Xiamen ( $9.10 \pm 5.70$  ppb h<sup>-1</sup>) and  
373 Shanghai (26 ppb h<sup>-1</sup>), while it was slightly higher than that in winter of Shanghai (~4 ppb h<sup>-1</sup>). The  
374 difference was strongly dependent on the precursor emissions and photochemical conditions of O<sub>3</sub>  
375 formation.

376 To examine the impacts of precursor emissions on O<sub>3</sub> production, RIR technique was applied  
377 to diagnose the O<sub>3</sub> sensitivity to precursors (Figure 8). First of all, all of the VOCs were classified  
378 into anthropogenic hydrocarbons (AHCs) and biogenic hydrocarbons (BHCs) (e.g., isoprene).  
379 Afterwards, all of AHCs could be further categorized into four groups of alkanes, alkenes, aromatics,  
380 and OVOCs. The O<sub>3</sub> production was highly VOC-sensitive especially AHCs-sensitive (RIR: 0.75),

381 followed by CO (0.21), and BHCs (0.12). However, the NO<sub>x</sub> showed the negative impact on O<sub>3</sub>  
382 production in Tangshan (RIR: -0.59). Among all of the AHCs, the contributions to O<sub>3</sub> sensitivity  
383 were in the order of alkenes (0.38) > OVOCs (0.27) > alkanes (0.18) > aromatics (0.09). The results  
384 also confirmed that the decreases of alkenes and OVOCs could alleviate O<sub>3</sub> pollution effectively.

#### 385 **4. Conclusions**

386 Due to the outbreak of COVID-19, many strict lockdown measures have been widely adopted across  
387 China, leading to dramatic decreases of vehicle and industrial emissions. Therefore, the  
388 concentrations of multiple air pollutants such as SO<sub>2</sub>, NO<sub>x</sub>, and CO experienced decreases during  
389 the pandemic, whereas the O<sub>3</sub> level suffered from significant increase. To uncover the reason for O<sub>3</sub>  
390 increase, the precursor concentrations (e.g., VOCs, NO<sub>x</sub>), meteorological conditions, and relevant  
391 chemical mechanisms have been analyzed. The ambient O<sub>3</sub> level increased by 143% during COVID-  
392 19 period, and the emission reduction and meteorology contributed to 77% and 66% of this  
393 increment, respectively. Along with the obvious increase of O<sub>3</sub> concentration, the VOC/NO<sub>x</sub> ratio  
394 also increased from 0.69 to 1.07 after COVID-19 lockdown, indicating the control of VOCs rather  
395 than NO<sub>x</sub> might be more effective in reducing O<sub>3</sub> level in Tangshan. In addition, the OFP values of  
396 VOC species were also calculated to assess their contributions to O<sub>3</sub> formation. We found that the  
397 alkenes and OVOCs displayed the higher contributions to O<sub>3</sub> production. Afterwards, a box model  
398 was applied to further analyze the detailed chemical mechanisms of O<sub>3</sub> formation and sensitivity.  
399 The result suggested that increased contributions of HO<sub>2</sub>+NO and RO<sub>2</sub>+NO resulted in the  
400 significant increase of O<sub>3</sub> concentration. Besides, the O<sub>3</sub> sensitivity analysis also demonstrated that  
401 the alkenes and OVOCs played significant roles on the O<sub>3</sub> formation. Thus, more efforts should be  
402 devoted to reduce the concentrations of alkenes and OVOCs.

#### 403 **Acknowledgements**

404 This work was supported by the National Natural Science Foundation of China (42107113).

#### 405 **Data availability**

406 The CEDS emission inventory are available at the website of  
407 <https://zenodo.org/record/3754964#.YwrJL8jfmfU>. The observed meteorological parameters are  
408 obtained from the website of <http://www.cma.gov.cn/>.

409

410 **References**

- 411 Chen, T., Xue, L., Zheng, P., Zhang, Y., Liu, Y., Sun, J., Han, G., Li, H., Zhang, X., Li, Y. (2020) Volatile  
412 organic compounds and ozone air pollution in an oil production region in northern China. *Atmospheric*  
413 *Chemistry and Physics* 20, 7069-7086.
- 414 Chen, Z., Zhuang, Y., Xie, X., Chen, D., Cheng, N., Yang, L., Li, R. (2019) Understanding long-term  
415 variations of meteorological influences on ground ozone concentrations in Beijing During 2006–2016.  
416 *Environmental pollution* 245, 29-37.
- 417 Dong, Y., Li, J., Guo, J., Jiang, Z., Chu, Y., Chang, L., Yang, Y., Liao, H. (2020) The impact of synoptic  
418 patterns on summertime ozone pollution in the North China Plain. *Science of the Total Environment*  
419 735, 139559.
- 420 Doumbia, T., Granier, C., Elguindi, N., Bouarar, I., Darras, S., Brasseur, G., Gaubert, B., Liu, Y., Shi, X.,  
421 Stavrakou, T. (2021) Changes in global air pollutant emissions during the COVID-19 pandemic: a  
422 dataset for atmospheric modeling. *Earth System Science Data* 13, 4191-4206.
- 423 Goldberg, D.L., Anenberg, S.C., Griffin, D., McLinden, C.A., Lu, Z., Streets, D.G. (2020) Disentangling  
424 the impact of the COVID-19 lockdowns on urban NO<sub>2</sub> from natural variability. *Geophysical Research*  
425 *Letters* 47, e2020GL089269.
- 426 Goldberg, D.L., Harkey, M., de Foy, B., Judd, L., Johnson, J., Yarwood, G., Holloway, T. (2022)  
427 Evaluating NO<sub>x</sub> emissions and their effect on O<sub>3</sub> production in Texas using TROPOMI NO<sub>2</sub> and  
428 HCHO. *Atmos. Chem. Phys.* 22, 10875-10900.
- 429 Gong, X., Hong, S., Jaffe, D.A. (2018) Ozone in China: Spatial distribution and leading meteorological  
430 factors controlling O<sub>3</sub> in 16 Chinese cities. *Aerosol and Air Quality Research* 18, 2287-2300.
- 431 Harrison, R.M., Allan, J., Carruthers, D., Heal, M.R., Lewis, A.C., Marner, B., Murrells, T., Williams, A.  
432 (2021) Non-exhaust vehicle emissions of particulate matter and VOC from road traffic: A review.  
433 *Atmospheric Environment* 262, 118592.
- 434 Hoesly, R.M., Smith, S.J., Feng, L., Klimont, Z., Janssens-Maenhout, G., Pitkanen, T., Seibert, J.J., Vu,  
435 L., Andres, R.J., Bolt, R.M. (2018) Historical (1750–2014) anthropogenic emissions of reactive gases  
436 and aerosols from the Community Emissions Data System (CEDS). *Geoscientific Model Development*  
437 11, 369-408.
- 438 Huang, X.-F., Wang, C., Zhu, B., Lin, L.-L., He, L.-Y. (2019) Exploration of sources of OVOCs in various  
439 atmospheres in southern China. *Environmental pollution* 249, 831-842.
- 440 Huang, X.-F., Zhang, B., Xia, S.-Y., Han, Y., Wang, C., Yu, G.-H., Feng, N. (2020) Sources of oxygenated  
441 volatile organic compounds (OVOCs) in urban atmospheres in North and South China. *Environmental*  
442 *pollution* 261, 114152.
- 443 Huang, X., Ding, A., Gao, J., Zheng, B., Zhou, D., Qi, X., Tang, R., Wang, J., Ren, C., Nie, W. (2021)  
444 Enhanced secondary pollution offset reduction of primary emissions during COVID-19 lockdown in  
445 China. *National Science Review* 8, nwaal37.
- 446 Hudman, R., Moore, N., Mebust, A., Martin, R., Russell, A., Valin, L., Cohen, R. (2012) Steps towards  
447 a mechanistic model of global soil nitric oxide emissions: implementation and space based-constraints.  
448 *Atmospheric Chemistry and Physics* 12, 7779-7795.
- 449 Jensen, A., Liu, Z., Tan, W., Dix, B., Chen, T., Koss, A., Zhu, L., Li, L., de Gouw, J. (2021) Measurements  
450 of volatile organic compounds during the COVID-19 lockdown in Changzhou, China. *Geophysical*  
451 *Research Letters* 48, e2021GL095560.
- 452 Jin, Z., Yezheng, W., Gang, Y. (2005) General formula for estimation of monthly average daily global  
453 solar radiation in China. *Energy Conversion and Management* 46, 257-268.

454 Li, M., Zhang, Q., Zheng, B., Tong, D., Lei, Y., Liu, F., Hong, C., Kang, S., Yan, L., Zhang, Y. (2019)  
455 Persistent growth of anthropogenic non-methane volatile organic compound (NMVOC) emissions in  
456 China during 1990–2017: drivers, speciation and ozone formation potential. *Atmospheric Chemistry  
457 and Physics* 19, 8897-8913.

458 Li, R., Xu, M., Li, M., Chen, Z., Zhao, N., Gao, B., Yao, Q. (2021a) Identifying the spatiotemporal  
459 variations in ozone formation regimes across China from 2005 to 2019 based on polynomial simulation  
460 and causality analysis. *Atmospheric Chemistry and Physics* 21, 15631-15646.

461 Li, R., Zhao, Y., Fu, H., Chen, J., Peng, M., Wang, C. (2021b) Substantial changes in gaseous pollutants  
462 and chemical compositions in fine particles in the North China Plain during the COVID-19 lockdown  
463 period: anthropogenic vs. meteorological influences. *Atmospheric Chemistry and Physics* 21, 8677-  
464 8692.

465 Li, X., Qin, M., Li, L., Gong, K., Shen, H., Li, J., Hu, J. (2022) Examining the implications of  
466 photochemical indicators on the O<sub>3</sub>-NO<sub>x</sub>-VOC sensitivity and control strategies: A case study in the  
467 Yangtze River Delta (YRD), China. *Atmos. Chem. Phys. Discuss.* 2022, 1-24.

468 Liu, T., Hong, Y., Li, M., Xu, L., Chen, J., Bian, Y., Yang, C., Dan, Y., Zhang, Y., Xue, L. (2022)  
469 Atmospheric oxidation capacity and ozone pollution mechanism in a coastal city of southeastern China:  
470 analysis of a typical photochemical episode by an observation-based model. *Atmospheric Chemistry  
471 and Physics* 22, 2173-2190.

472 Liu, X., Lyu, X., Wang, Y., Jiang, F., Guo, H. (2019) Intercomparison of O<sub>3</sub> formation and radical  
473 chemistry in the past decade at a suburban site in Hong Kong. *Atmospheric Chemistry and Physics* 19,  
474 5127-5145.

475 Louie, P.K., Ho, J.W., Tsang, R.C., Blake, D.R., Lau, A.K., Yu, J.Z., Yuan, Z., Wang, X., Shao, M., Zhong,  
476 L. (2013) VOCs and OVOCs distribution and control policy implications in Pearl River Delta region,  
477 China. *Atmospheric Environment* 76, 125-135.

478 Maji, S., Beig, G., Yadav, R. (2020) Winter VOCs and OVOCs measured with PTR-MS at an urban site  
479 of India: role of emissions, meteorology and photochemical sources. *Environmental pollution* 258,  
480 113651.

481 Mozaffar, A., Zhang, Y.-L. (2020) Atmospheric volatile organic compounds (VOCs) in China: a review.  
482 *Current Pollution Reports* 6, 250-263.

483 Murray, L.T., Jacob, D.J., Logan, J.A., Hudman, R.C., Koshak, W.J. (2012) Optimized regional and  
484 interannual variability of lightning in a global chemical transport model constrained by LIS/OTD  
485 satellite data. *Journal of Geophysical Research: Atmospheres* 117.

486 Ning, G., Yim, S.H.L., Yang, Y., Gu, Y., Dong, G. (2020) Modulations of synoptic and climatic changes  
487 on ozone pollution and its health risks in mountain-basin areas. *Atmospheric Environment* 240, 117808.

488 Nussbaumer, C.M., Pozzer, A., Tadic, I., Röder, L., Obersteiner, F., Harder, H., Lelieveld, J., Fischer, H.  
489 (2022) Tropospheric ozone production and chemical regime analysis during the COVID-19 lockdown  
490 over Europe. *Atmos. Chem. Phys.* 22, 6151-6165.

491 Saha, L., Kumar, A., Kumar, S., Korstad, J., Srivastava, S., Baudh, K. (2022) The impact of the COVID-  
492 19 lockdown on global air quality: A review. *Environmental Sustainability*, 1-19.

493 Shi, X., Brasseur, G.P. (2020) The response in air quality to the reduction of Chinese economic activities  
494 during the COVID-19 outbreak. *Geophysical Research Letters* 47, e2020GL088070.

495 Shu, L., Wang, T., Han, H., Xie, M., Chen, P., Li, M., Wu, H. (2020) Summertime ozone pollution in the  
496 Yangtze River Delta of eastern China during 2013–2017: Synoptic impacts and source apportionment.  
497 *Environmental pollution* 257, 113631.

498 Song, C., Liu, Y., Sun, L., Zhang, Q., Mao, H. (2020) Emissions of volatile organic compounds (VOCs)  
499 from gasoline-and liquified natural gas (LNG)-fueled vehicles in tunnel studies. *Atmospheric*  
500 *Environment* 234, 117626.

501 Tang, W., Yang, K., He, J., Qin, J. (2010) Quality control and estimation of global solar radiation in China.  
502 *Solar Energy* 84, 466-475.

503 Van Der Werf, G.R., Randerson, J.T., Giglio, L., Van Leeuwen, T.T., Chen, Y., Rogers, B.M., Mu, M.,  
504 Van Marle, M.J., Morton, D.C., Collatz, G.J. (2017) Global fire emissions estimates during 1997–2016.  
505 *Earth System Science Data* 9, 697-720.

506 Venter, Z.S., Aunan, K., Chowdhury, S., Lelieveld, J. (2020) COVID-19 lockdowns cause global air  
507 pollution declines. *Proceedings of the National Academy of Sciences* 117, 18984-18990.

508 Wang, M., Lu, S., Shao, M., Zeng, L., Zheng, J., Xie, F., Lin, H., Hu, K., Lu, X. (2021) Impact of COVID-  
509 19 lockdown on ambient levels and sources of volatile organic compounds (VOCs) in Nanjing, China.  
510 *Science of the Total Environment* 757, 143823.

511 Wang, M., Qin, W., Chen, W., Zhang, L., Zhang, Y., Zhang, X., Xie, X. (2020a) Seasonal variability of  
512 VOCs in Nanjing, Yangtze River delta: Implications for emission sources and photochemistry.  
513 *Atmospheric Environment* 223, 117254.

514 Wang, P., Yang, Y., Li, H., Chen, L., Dang, R., Xue, D., Li, B., Tang, J., Leung, L.R., Liao, H. (2022)  
515 North China Plain as a hot spot of ozone pollution exacerbated by extreme high temperatures.  
516 *Atmospheric Chemistry and Physics* 22, 4705-4719.

517 Wang, Y., Wen, Y., Wang, Y., Zhang, S., Zhang, K.M., Zheng, H., Xing, J., Wu, Y., Hao, J. (2020b) Four-  
518 month changes in air quality during and after the COVID-19 lockdown in six megacities in China.  
519 *Environmental Science & Technology Letters* 7, 802-808.

520 Wu, C., Wang, C., Wang, S., Wang, W., Yuan, B., Qi, J., Wang, B., Wang, H., Wang, C., Song, W. (2020)  
521 Measurement report: Important contributions of oxygenated compounds to emissions and chemistry  
522 of volatile organic compounds in urban air. *Atmospheric Chemistry and Physics* 20, 14769-14785.

523 Xue, L., Gu, R., Wang, T., Wang, X., Saunders, S., Blake, D., Louie, P.K., Luk, C.W., Simpson, I., Xu,  
524 Z. (2016) Oxidative capacity and radical chemistry in the polluted atmosphere of Hong Kong and Pearl  
525 River Delta region: analysis of a severe photochemical smog episode. *Atmospheric Chemistry and*  
526 *Physics* 16, 9891-9903.

527 Yin, Z., Wan, Y., Wang, H. (2021) Decadal changes of connections among late-spring snow cover in West  
528 Siberia, summer Eurasia teleconnection and O<sub>3</sub>-related meteorology in North China. *Atmos. Chem.*  
529 *Phys.* 21, 11519-11530.

530 Zhang, K., Liu, Z., Zhang, X., Li, Q., Jensen, A., Tan, W., Huang, L., Wang, Y., de Gouw, J., Li, L. (2022a)  
531 Insights into the significant increase in ozone during COVID-19 in a typical urban city of China.  
532 *Atmospheric Chemistry and Physics* 22, 4853-4866.

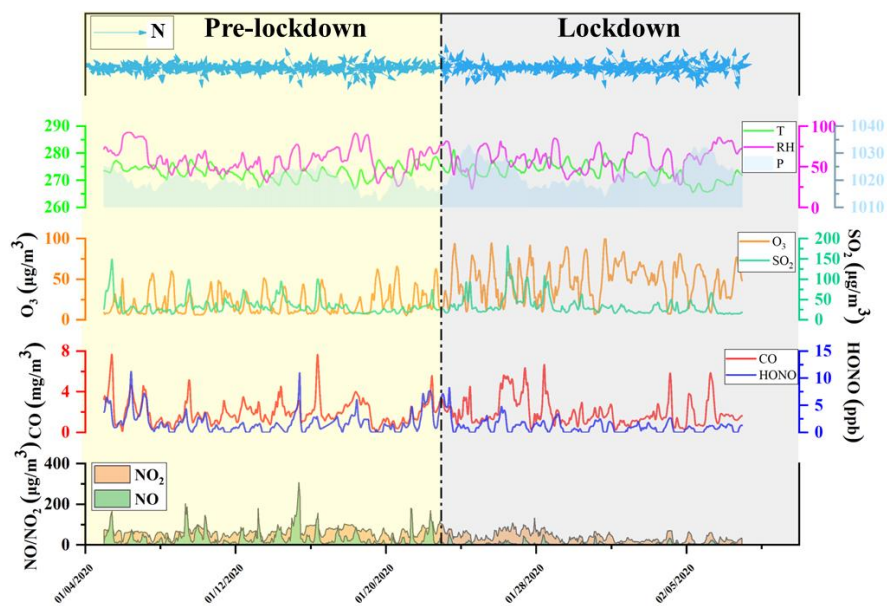
533 Zhang, X., Yin, Y., van der A, R., Eskes, H., van Geffen, J., Li, Y., Kuang, X., Lapierre, J.L., Chen, K.,  
534 Zhen, Z., Hu, J., He, C., Chen, J., Shi, R., Zhang, J., Ye, X., Chen, H. (2022b) Influence of convection  
535 on the upper-tropospheric O<sub>3</sub> and NO<sub>x</sub> budget in southeastern China. *Atmos. Chem. Phys.* 22, 5925-  
536 5942.

537 Zhang, Z., Zhang, Y., Wang, X., Lü, S., Huang, Z., Huang, X., Yang, W., Wang, Y., Zhang, Q. (2016)  
538 Spatiotemporal patterns and source implications of aromatic hydrocarbons at six rural sites across  
539 China's developed coastal regions. *Journal of Geophysical Research: Atmospheres* 121, 6669-6687.

540 Zhao, Y., Zhang, K., Xu, X., Shen, H., Zhu, X., Zhang, Y., Hu, Y., Shen, G. (2020) Substantial changes  
541 in nitrogen dioxide and ozone after excluding meteorological impacts during the COVID-19 outbreak

542 in mainland China. *Environmental Science & Technology Letters* 7, 402-408.  
543 Zheng, B., Zhang, Q., Geng, G., Shi, Q., Lei, Y., He, K. (2020) Changes in China's anthropogenic  
544 emissions during the COVID-19 pandemic. *Earth System Science Data Discussions* 10.  
545 Zhou, Y., Cheng, S., Chen, D., Lang, J., Zhao, B., Wei, W. (2014) A new statistical approach for  
546 establishing high-resolution emission inventory of primary gaseous air pollutants. *Atmospheric*  
547 *Environment* 94, 392-401.

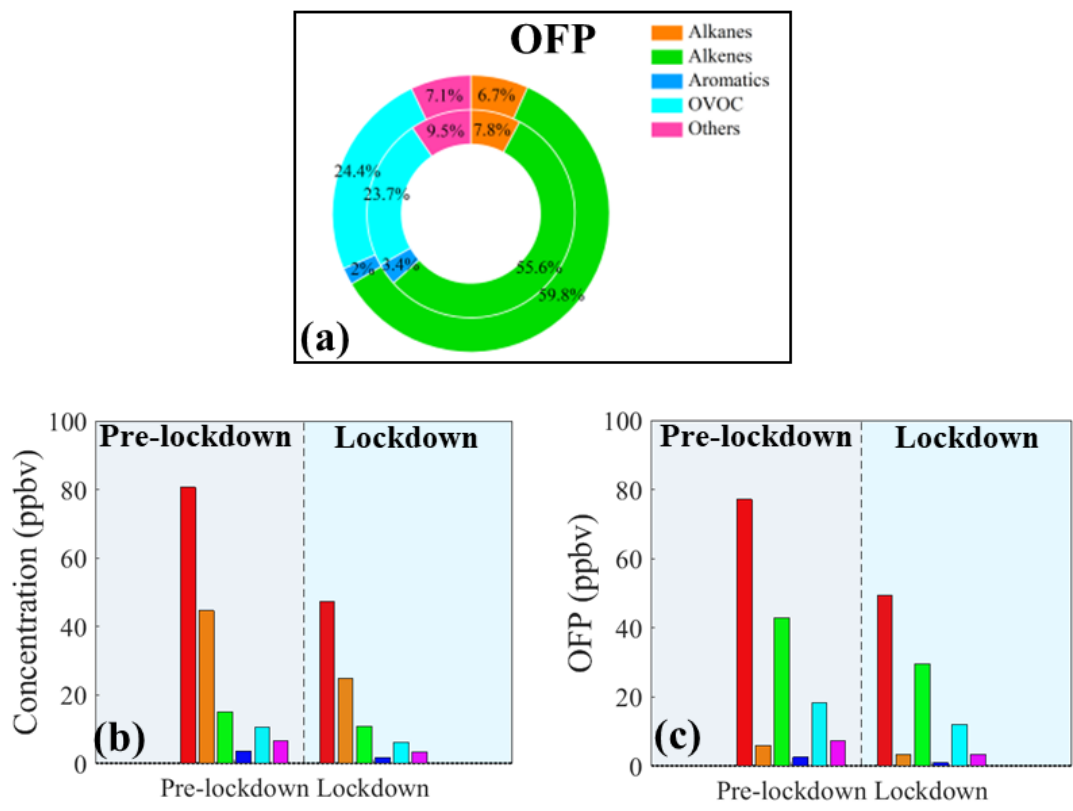
548 **Figure 1** Temporal variations of meteorological parameters (e.g., T, RH, P) and gaseous pollutants  
549 (e.g., SO<sub>2</sub>, O<sub>3</sub>) during the whole observation. The date is shown in the format month/day/year.



550

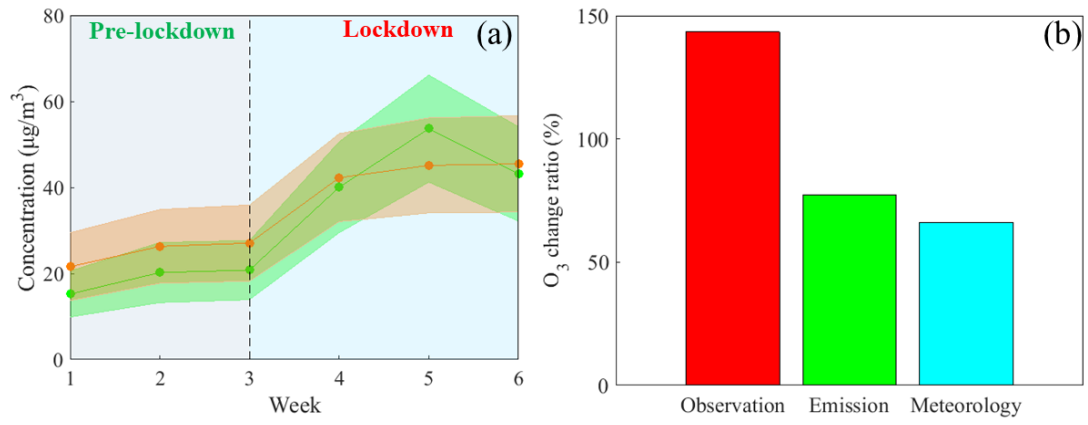
551

552 **Figure 2** The OFP contribution ratios of VOC species (a). The absolute concentrations (b) and OFP  
 553 values (c) during pre-lockdown and lockdown periods.



554

555 **Figure 3** Comparison of observed O<sub>3</sub> (green) and normalized O<sub>3</sub> concentrations (orange) during  
556 pre-lockdown and lockdown periods (a). The O<sub>3</sub> change ratios derived from observation, emission,  
557 and meteorology.

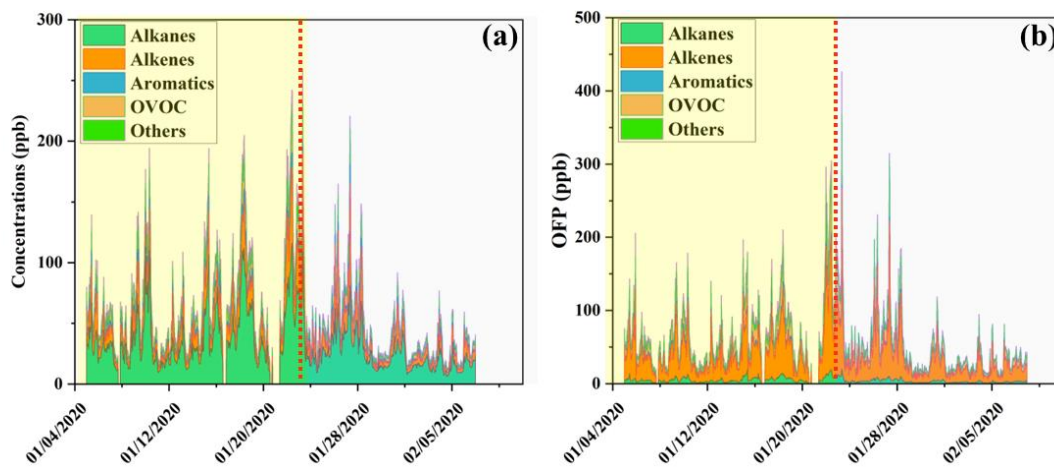


558

559

560

561 **Figure 4** The temporal variations of absolute concentrations (a) and OFP (b) for VOC species during  
562 the whole sampling period. The yellow and white episodes represent the pre-lockdown and  
563 lockdown periods.

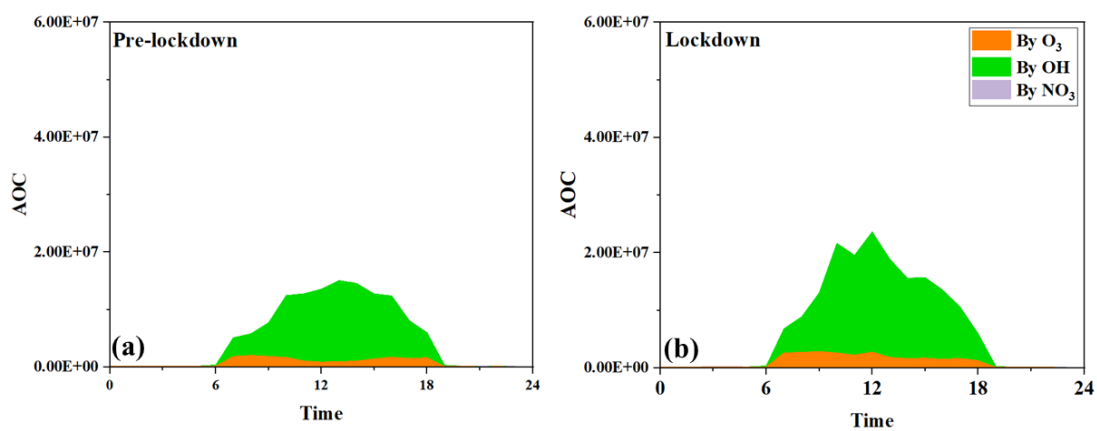


564

565

566

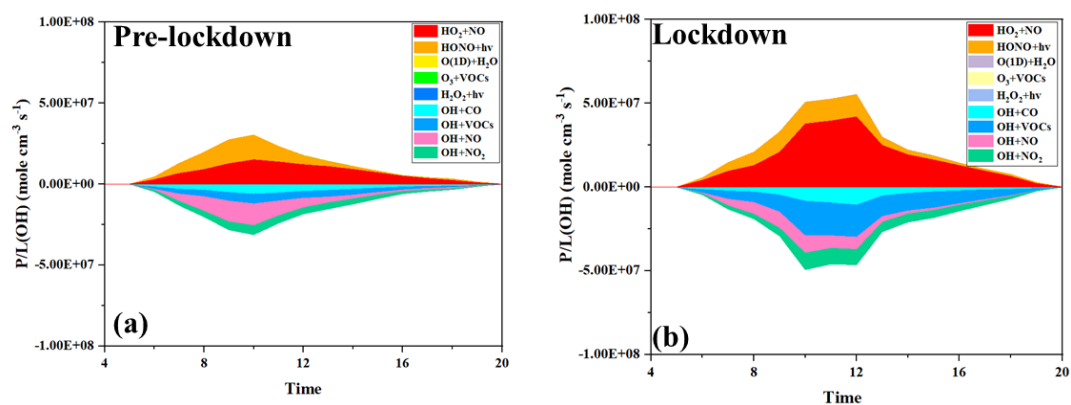
567 **Figure 5** Hourly variations of model-estimated AOC contributed by O<sub>3</sub>, OH, and NO<sub>3</sub> radical during  
568 pre-lockdown and lockdown periods (Unit: molecules cm<sup>-3</sup>).



569

570

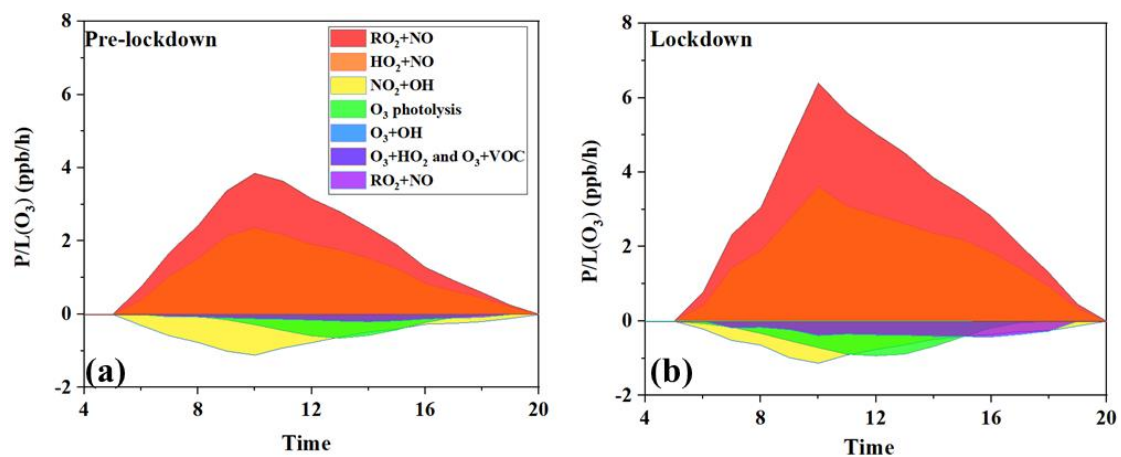
571 **Figure 6** Daytime variation of OH budget during pre-lockdown and lockdown periods.



572

573

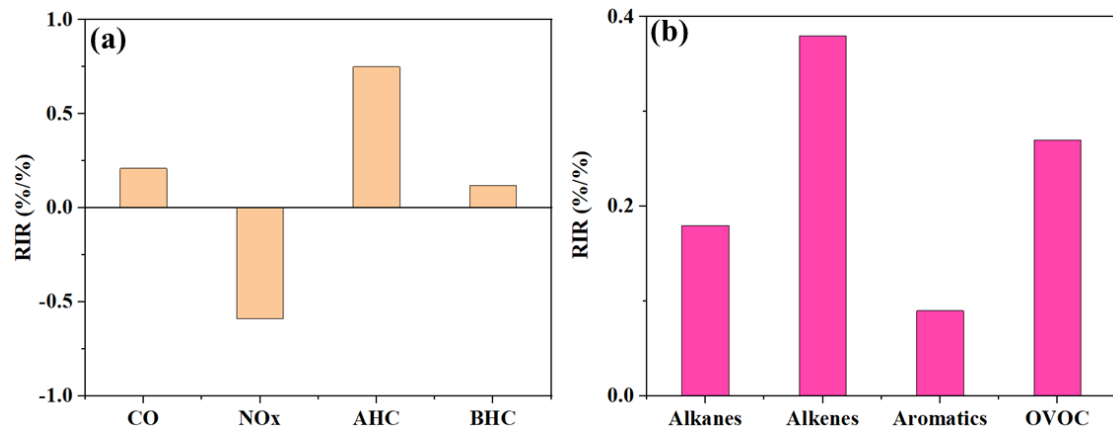
574 **Figure 7** Daytime variation of O<sub>3</sub> budget during pre-lockdown and lockdown periods.



575

576

577 **Figure 8** The model-estimated RIR values for major O<sub>3</sub> precursor groups and (b) the sub-groups of  
578 anthropogenic VOC species.



579

580

581